ACS OMEGA

http://pubs.acs.org/journal/acsodf

Article

Effect of Hydration on the Molecular Dynamics of Hydroxychloroquine Sulfate

Eugene Mamontov,* Yongqiang Cheng, Luke L. Daemen, Jong K. Keum, Alexander I. Kolesnikov, Daniel Pajerowski, Andrey Podlesnyak, Anibal J. Ramirez-Cuesta, Matthew R. Ryder, and Matthew B. Stone

Cite This: *ACS Omega* 2020, 5, 21231−21240

Read Online

ACCESS | Metrics & More | Article Recommendations | Supporting Information

ABSTRACT: Chloroquine and its derivative hydroxychloroquine are primarily known as antimalaria drugs. Here, we investigate the influence of hydration water on the molecular dynamics in hydroxychloroquine sulfate, a commonly used solubilized drug form. When hydration, even at a low level, results in a disordered structure, as opposed to the highly ordered structure of dry hydroxychloroquine sulfate, the activation barriers for the rotation of methyl groups in the drug molecules become randomized and, on average, significantly reduced. The facilitated stochastic motions of the methyl groups may benefit the biomolecular activity due to the more efficient sampling of the energy landscape in the disordered hydration environment experienced by the drug molecules *in vivo*.

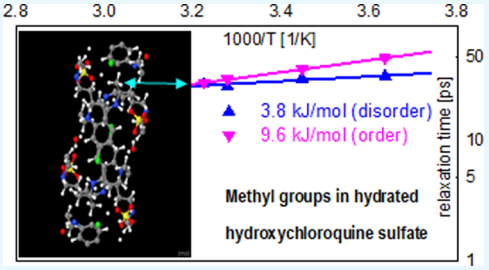

INTRODUCTION

Chloroquine (CQ) and its derivative hydroxychloroquine (HCQ) are drug molecules that have been used for malaria treatment and also as immunosuppressants in the treatment of autoimmune disorders such as rheumatoid arthritis and lupus.[1] The drugs have also been suggested as promising agents for antitumor therapy.[2,3] However, they have recently attracted attention and debate as potential antiviral drugs,[4] coming to prominence from the coronavirus disease (COVID-19) caused by SARS-CoV-2. Given the conflicting evidence of CQ and HCQ efficacy for the treatment of COVID-19 and the potential adverse side effects,[5−7] their use and further trials are currently restricted to clinical settings under strict medical supervision due to safety considerations.

The therapeutic action of CQ and HCQ tends to be closely linked to their protonation and deprotonation. These compounds preferentially accumulate in the lysosomes and endosomes of cells, increasing the pH of the environment. This inhibits the processes such as autophagy or virus release from the endosome or lysosome since these processes require acidic conditions. In antiviral therapies, this inhibition may impede the ability of the virus to release its genetic material into the cell.[4] The accumulation of CQ and HCQ in lysosomes, which is due to their basic properties, may result in a 100- to 1000-fold increase in the concentration of these drugs compared to the plasma or cytosol concentration.[8,9] Thus, these drugs may be present in the organism in aqueous environments at vastly different levels.

The influence of aqueous hydration on the molecular dynamics and, ultimately, the function of biomolecules has been widely recognized. Such influence can be very broad, as hydration-dependent enabling of the general enzymatic activity by proteins,[10] or specific and crucial, as control of kinetic proofreading in the aminoacylation of RNA.[11] Importantly, even the small-amplitude molecular motions can have a critical influence on the biological function. For example, a static picture of a transmembrane protein cannot adequately describe the function of Gramicidin A and KcsA potassium channels without taking into consideration their thermal atomic motions with sub-Angstrom amplitude that play a decisive role in facilitating or blocking ion transmission.[12] Such thermal fluctuations with sub-Angstrom amplitude can be probed efficiently by inelastic (INS) and quasielastic (QENS) neutron scattering. While the crystallographic structure of chloroquine-based compounds has been studied extensively,[13] the molecular dynamics have yet to be investigated. In this work, we employ neutron scattering techniques to probe the influence of hydration water on the molecular dynamics in HCQ sulfate (HCQS), a commonly used drug of the chloroquine family. The structure of HCQ and HCQS units is presented schematically in Figure 1.

The protons of H_2SO_4 attach to two of the nitrogen atoms of hydroxychloroquine, resulting in the formation of a hydroxychloroquine cation and a sulfate anion. Thus, unlike the free base HCQ, HCQS is readily solvable in water. While free base hydroxychloroquine ($C_{18}H_{26}ClN_3O$, CAS number 118-42-3)

Received: June 26, 2020
Accepted: July 24, 2020
Published: August 10, 2020

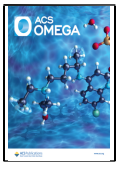

https://dx.doi.org/10.1021/acsomega.0c03091
ACS Omega 2020, 5, 21231−21240

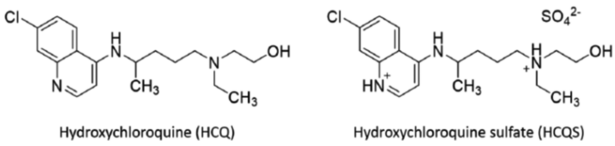

Figure 1. Schematic representation of hydroxychloroquine (left) and hydroxychloroquine sulfate (right).

has limited solubility in water of only 0.0261 mg/mL,[14] hydroxychloroquine sulfate (HCQS) ($C_{18}H_{26}ClN_3O_5H_2SO_4$, CAS number 747-36-4) is readily solvable at least at 20 mg/mL and as high as 87 mg/mL at 25 °C (200.48 mM).[15]

RESULTS AND DISCUSSION

For the preparation of hydrated solid HCQS samples, various approaches have been attempted. It should be noted that, despite a high solubility in water, the HCQS powder was not found to be hygroscopic and did not show any weight uptake when exposed to ambient humidity for 7 days. This is in remarkable contrast with the hydration behavior of powders of inorganic hydrophilic compounds[16] and lyophilized biomolecules,[17,18] which readily adsorb water from ambient vapor in amounts sufficient for the adsorbed hydration water to exhibit bulk-like traits of microscopic dynamics, albeit without crystallization on cooling. HCQS powder was dissolved in water at 20 mg/mL in an open glass Petri dish. The water was then allowed to evaporate in a chemical fume hood for 96 h. The resulting residue was transparent and had a hardened epoxy appearance, which could be scraped from the dish with a steel spatula. The weight uptake was ∼16.7%; this value was repeatedly achieved when preparing several samples and therefore indicated a sample composition of $C_{18}H_{26}ClN_3O_5H_2SO_4(H_2O)_4$, with four water molecules per HCQS molecular unit. We hypothesize that this composition represents a stable low-hydration state of HCQS. Interestingly, when the HCQS powder was initially dissolved in water, before obtaining a fully mixed solution, dense regions with filamentary structures with the appearance of the hydrated epoxy-like sample were observed. For the main hydrated solid sample, 0.54 g of the $C_{18}H_{26}ClN_3O_5H_2SO_4(H_2O)_4$ was used. Before the scattering measurements occurred, this main hydrated solid sample was kept inside the sealed sample holder at 310 K for 12 h. A second, less ordered, hydrated solid sample with the same composition was then prepared similarly to the main sample, except that it was not annealed inside the sealed sample holder at 310 K before the measurements. A third, more ordered, hydrated solid sample was prepared by mixing the HCQS powder with a stoichiometric amount of water to achieve a targeted composition of $C_{18}H_{26}ClN_3O_5H_2SO_4(H_2O)_4$ and then loaded into a similar sealed sample holder. This approach was previously used[19] to achieve the desired hydration level and behavior in inorganic powders similar to those obtained using vapor.[16] Besides the hydrated solid samples, 0.46 g dry HCQS was loaded into a similarly sealed sample holder. For a subset of measurements, a 0.56 g sample of free base hydroxychloroquine, $C_{18}H_{26}ClN_3O_5$ (HCQ), was also loaded into a similarly sealed sample holder. Neutron scattering measurements were performed at several spectrometers at the Spallation Neutron Source (SNS) at the Oak Ridge National Laboratory (ORNL): BASIS,[20] SEQUOIA,[21] VISION,[22] and CNCS.[23]

Diffusion in aqueous solutions of HCQS was analyzed using QENS data from BASIS (Figures S1 and S2). The resulting diffusivity values are displayed in Figure 2 and exhibit similar activation energies for the 20 and 40 mg/mL solutions of 18.9

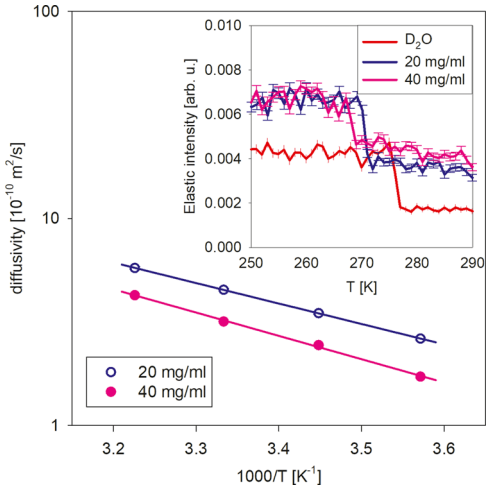

Figure 2. Diffusivity values in 20 and 40 mg/mL aqueous solutions of HCQS measured at BASIS (the error bars are within the symbols). The solid lines are linear fits to extract the activation energy, as described in the text. Inset: temperature-dependent scans of the wave-vector integrated elastic neutron scattering intensity showing freezing point depression of the solutions compared to the D_2O buffer.

and 21.5 kJ/mol (linear fits in Figure 2), respectively. Since the data that we have fitted following subtraction of the D_2O buffer signal did not support the presence of more than one dynamic component, the measured QENS dynamics in solutions were either similar between the cations and anions or completely dominated by the motion of one species, more likely the cations. Even if the hydrated SO_4 anions were strongly dissociated from the HCQ cations (also hydrated) and their diffusivities were substantially different, the relatively much larger number of hydrogens associated with the hydrated HCQ cations would seem to suggest the cation dominance in the measured scattering signal. Furthermore, the diffusivity values reported herein are likely related to global (combined translational and rotational) motion of the solute species, whereas the actual translation diffusivity values are somewhat lower. For example, for the particles that could be approximated by the dense, hard spheres, the global diffusion coefficient measured by QENS would exceed the actual translational diffusion coefficient by ca. 27%.[24]

The internal dynamics of HCQS molecules were probed using the solid samples. From the neutron diffraction patterns measured at SEQUOIA and CNCS (Figure S3), the structures of dry HCQS and more ordered hydrated HCQS look similar, as their features almost overlap after subtraction of a constant from the latter to account for the higher incoherent scattering background from the hydrated sample. The structures of the main hydrated HCQS and less ordered hydrated HCQS are similar to one another (although the latter exhibits somewhat less prominent diffraction peaks) but differ from the dry and more ordered hydrated HCQS. The CNCS data demonstrates larger mean-squared displacements (MSD) at 310 K in the main hydrated sample compared to the dry, as evidenced by the relatively faster decrease with Q of the data baseline that represents the incoherent scattering signal from the protons. The diffraction data in Figure S3 suggest that the hydration of

https://dx.doi.org/10.1021/acsomega.0c03091
ACS Omega 2020, 5, 21231−21240

the main and the less ordered samples resulted in the formation of a different structure.

The INS spectra of dry HCQS, measured at VISION and calculated using density functional theory (DFT), are presented in Figure 3. The DFT results agree well with the experiment and

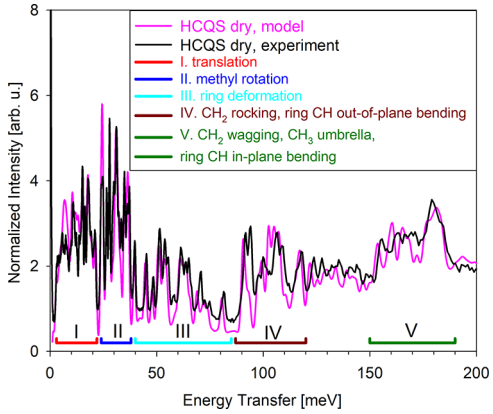

Figure 3. INS spectra of dry HCQS measured on VISION (black) and computed using DFT (pink). The assignments of vibration modes, according to the DFT results, are represented below the spectra and in the corresponding colored legend.

thus allow for a reliable assignment of the vibrational modes. Figure 4 shows the measured spectra of dry and main hydrated

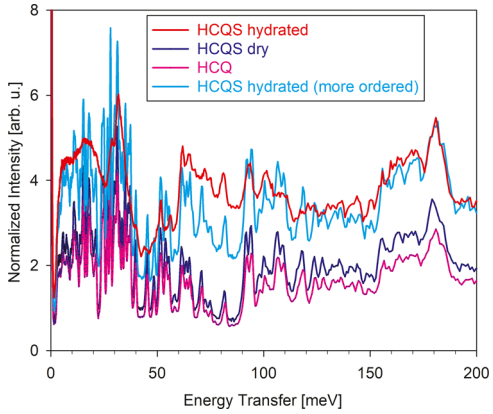

Figure 4. INS spectra of dry (blue) and main hydrated (red) hydroxychloroquine sulfate as well as free base hydroxychloroquine (pink, scaled to the same mole values as the other two samples) and more ordered hydrated (cyan) hydroxychloroquine sulfate measured on the VISION spectrometer.

HCQS as well as more ordered HCQS and free base HCQ. While the difference between dry HCQS and HCQ, introduced by the protonation of HCQ and the presence of the sulfate anion, appears limited, the effect of hydration (at a similar level) on the vibrational spectra differs dramatically between the main hydrated HCQS and more ordered hydrated HCQS.

The latter system, which retains the structure of dry HCQS (Figure S3), exhibits a vibrational pattern similar to HCQ and dry HCQS, albeit with a higher background due to the water. On the contrary, the main hydrated HCQS exhibits a very different hydration pattern in the low-energy range, below ~60 meV, indicating significant disorder within the sample. Note that Figure 4 is intended to make a comparison among the overall vibrational patterns and their relative intensities, whereas the low-energy range will be plotted separately over an expanded energy range and discussed in more detail below. The data in Figure 4 suggest that the main hydrated HCQS sample not only has a different crystallographic structure, as evidenced by the diffraction data in Figure S3, but indeed becomes less ordered. The INS data collected at SEQUOIA also supports this conclusion.

QENS measurements on BASIS were used to probe the relaxation dynamics in dry and main hydrated HCQS at physiological (body) temperature. The results for the mean-squared displacements (Figure S4) are in agreement with the trend evident from Figure S3, showing that the displacements for the main hydrated sample exhibit a much stronger temperature dependence. While both dry and the main hydrated HCQS samples show a sustained increase in the mean-squared displacements above 100 K, the latter also exhibits an additional, faster increase with temperature above 250 K. Therefore, a relatively more complex, possibly multicomponent scenario of dynamic processes in the main hydrated HCQS sample at physiological temperatures could be inferred. This is indeed confirmed by a comparison of the QENS spectra for the dry and main hydrated samples, as presented in Figure 5.

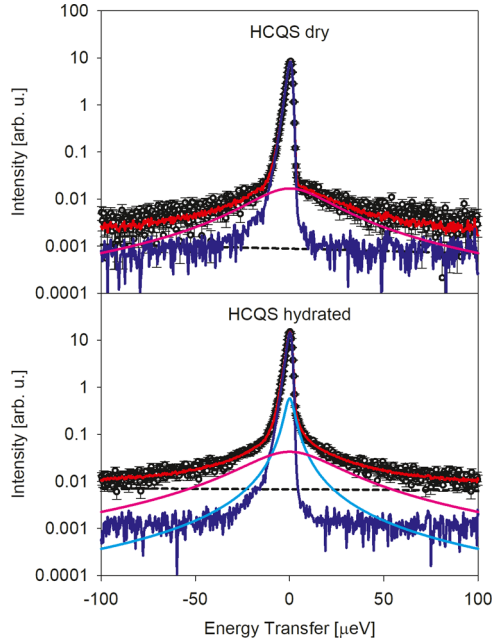

Figure 5. QENS spectra of the dry (top) and main hydrated (bottom) HCQS samples measured using the BASIS spectrometer at 310 K at $Q = 0.3$ Å^{-1}. Red solid line: overall fit. Deep blue solid line: elastic component of the fit. Pink and cyan solid lines: quasielastic components of the fit. Dashed line: background component of the fit.

The spectra feature a prominent elastic line and quasielastic wings. The dry HCQS spectra can be adequately fitted with the expression

$$I(Q, E) = \left[x(Q)\delta(E) + (1 - x(Q))\frac{1}{\pi}\frac{\Gamma(Q)}{\Gamma(Q)^2 + E^2}\right] \otimes R(Q, E) + (C_1(Q)E + C_2(Q)) \quad (1)$$

where the fraction of the elastic scattering signal, $x(Q)$, represents the elastic incoherent structure factor (EISF), $\Gamma(Q)$ is the half-width at half maximum (HWHM) of the Lorentzian

https://dx.doi.org/10.1021/acsomega.0c03091
ACS Omega 2020, 5, 21231−21240

quasielastic component, $R(Q, E)$ is the experimentally measured resolution function numerically convolved with a superposition of the delta-function (elastic) and Lorentzian (quasielastic) components, and the term in the parentheses represents a fitted linear background. On the other hand, the spectra collected from the main hydrated HCQS sample, in the bottom panel of Figure 5, require two quasielastic components, broad and narrow, as follows

$$I(Q, E) = \Bigg[x(Q)\delta(E) + (1 - x(Q)) \left(y(Q)\frac{1}{\pi}\frac{\Gamma_n(Q)}{\Gamma_n(Q)^2 + E^2} + (1 - y(Q)) \frac{1}{\pi}\frac{\Gamma_b(Q)}{\Gamma_b(Q)^2 + E^2}\right)\Bigg] \otimes R(Q, E) + (C_1(Q)E + C_2(Q)) \quad (2)$$

To better illustrate this, in Figure 6 we present the same data as plotted in Figure 5, but with the scattering and fitted intensities

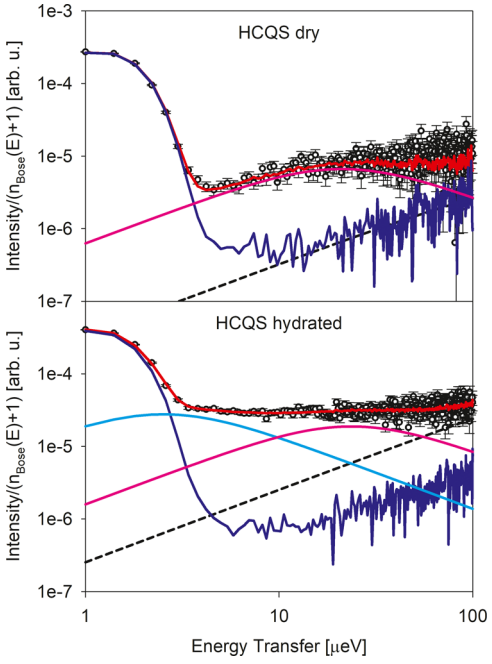

Figure 6. Same $I(Q, E)$ data as presented in Figure 5 but renormalized as $I(Q, E)/(n_{\mathrm{Bose}}(E) + 1)$.

renormalized as $I(Q, E)/(n_{\mathrm{Bose}}(E) + 1)$, where $n_{\mathrm{Bose}}(E) = (\exp(E/k_{\mathrm{B}}T) - 1)^{-1}$ is Bose population factor and k_{B} is Boltzmann's constant. At higher-energy transfers, where the influence of the spectrometer resolution is relatively weak, such renormalized data approximates the imaginary part of the dynamic susceptibility, $\chi''(Q, E)$. The maxima of dynamic susceptibility correspond to the characteristic relaxation frequencies in the system, thus enabling intuitive visualization.

One can see that for the main hydrated HCQS sample, an additional fit component (cyan solid line) is indeed necessitated by the deviation of the low-energy data points (symbols) from the elastic signal (deep blue solid line). Addition of the second fit component results in a good overall fit to the data (red solid line).

The HWHMs of the QENS components (Figure S5) in the energy range of 10−30 μeV exhibit only a relatively weak Q-dependence, indicative of localized, as opposed to translational, dynamic processes, whereas the additional narrow (2−3 μeV) component in the main hydrated HCQS sample has no significant Q-dependence. This narrow component could be ascribed to the dynamics of the water molecules. The width of the broad component is similar for the dry and hydrated samples at 310 K. However, the temperature dependence is quite different, as it is much more pronounced and systematic in the dry sample. The corresponding Arrhenius plot, with relaxation times calculated from the Q-averaged QENS broadening values as $\tau = \hbar/\langle \mathrm{HWHM}(Q)\rangle$, is presented in Figure 7. Also shown are

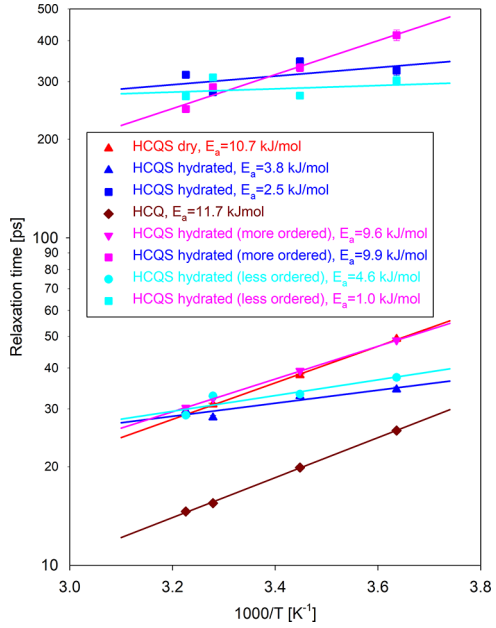

Figure 7. Arrhenius plot of the relaxation times (symbols) and fits (lines) for the dynamic process in dry HCQS and two dynamic processes in the main hydrated HCQS sample. Also presented are the data for the free base HCQ (one dynamic process) and the more ordered and less ordered hydrated HCQS samples (two dynamic processes). The square symbols (at longer relaxation times) represent the hydration water. When not visible, the error bars are within the size of the symbol.

the relaxation times for the more ordered and less ordered hydrated samples obtained in the same way as for the main hydrated sample. It is immediately evident that much smaller activation energies are observed for the main hydrated and less ordered hydrated samples (blue and cyan symbols and lines). At first, we discuss the principal dynamic component, which is represented by the symbols other than squares (whereas the squares represent the dynamic component associated with the hydration water). There is only a relatively small difference in the activation energy between the dry HCQS and free base HCQ. The latter is also characterized by a single-component QENS signal, just as dry HCQS. Furthermore, the more ordered hydrated HCQS sample also exhibits similar activation energy.

On the other hand, hydration in the main and less ordered HCQS samples reduces the activation energy by about a factor of 2.5−3.0. For the main hydrated sample, this reduced activation energy value becomes comparable with the low activation energy exhibited by its hydration water (longer relaxation times, square symbols, in Figure 7). At the same time,

https://dx.doi.org/10.1021/acsomega.0c03091
ACS Omega 2020, 5, 21231−21240

the activation energy exhibited by the hydration water in the less ordered hydrated sample is even lower. Interestingly, the activation energy exhibited by the water in the more ordered hydrated sample is essentially the same as that of the principal dynamic component in this sample, suggesting that the motion of the hydration water molecules is highly correlated with the motion of other entities in this sample. This is corroborated by the INS data measured up to 50 meV at SEQUOIA (Figure S6), which exhibit very similar features for the dry and more ordered hydrated sample, in contrast with the typical behavior of surface/interfacial water.[25]

While the dynamic component associated with longer relaxation times (square symbols in Figure 7) can be ascribed to the hydration water molecules, the origin of the main dynamic component warrants further discussion. To this end, the EISF(Q) at 310 K is fitted (Figure 8) with an expression for

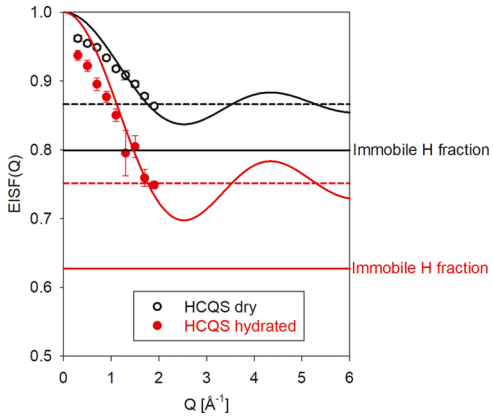

Figure 8. Fits using eq 3 of the momentum transfer-dependent elastic incoherent structure factor, EISF(Q), data measured at BASIS at 310 K for the dry (black) and main hydrated HCQS (red) samples. The solid horizontal lines indicate the fraction of the immobile hydrogens (parameter c in eq 3). The dashed horizontal lines are drawn at the values of $c + (1 - c)/3$.

3-fold jumps[26] on a circle of radius r modified to allow for an additional parameter, c, describing the fraction of the immobile particles

$$\mathrm{EISF}(Q) = c + (1 - c)(1 + 2j_0(Qr\sqrt{3}))/3 \quad (3)$$

where j_0 is a spherical Bessel function of zeroth order. Using a known value of 1.78 Å for the proton−proton distance in methyl groups, which corresponds to $r = 1$ Å in eq 3, the fits shown with the solid lines in Figure 8 were obtained with a single fit parameter, c, whose value is represented by a solid horizontal line. The fitted curve oscillates about the value of $c + (1- c)/3$ since for 3-fold jumps on a circle, the EISF(Q) should asymptotically approach a value of 1/3 at high Q values.[26] It should be noted that fitting the EISF(Q) with any generic model, such as motion on a sphere or within a spherical volume, shows the same deviation at the lower Q values between the fits approaching unity and the data points positioned below the fit curve. This indicates not the inadequacy of the 3-fold jump model, but rather a systematic error in the EISF(Q) data in the low-Q region, which is known to originate from multiple scattering in the sample.[27] Indeed, the discrepancy becomes more pronounced for the main hydrated HCQS sample, as one would expect for the stronger scattering sample with more pronounced multiple scattering effects. It should be noted that some multiple scattering, especially in the main hydrated HCQS sample, was unavoidable due to the sample morphology (hardened epoxy), which precluded the use of a sample holder less than 1.0 mm in thickness. With the flat-plate sample oriented perpendicular to the incident neutron beam, the first five Q values are measured in transmission geometry and are especially susceptible to multiple scattering effects.

Nevertheless, there are several compelling reasons to ascribe the broad dynamic component to the rotation of methyl groups in HCQS. First, the fitted values of the "immobile fraction" parameter c of 0.799 ± 0.003 and 0.627 ± 0.007 for the dry and main hydrated sample are in excellent agreement with the values one would expect from the two rotating methyl groups with six hydrogens per molecule, $(28 - 6)/28 = 0.79$ for the dry HCQS (with a total of 28 hydrogens per molecule) and $(36 - 8 - 6)/36 = 0.61$ for the hydrated HCSQ (with a total of 36 hydrogens per molecule, out of which the eight hydrogens associated with the four H_2O units are mobile). Second, the activation energy of 10.7 kJ/mol, or 111 meV, determined from the Arrhenius plot for the broad dynamic component in dry HCQS in Figure 7 predicts the first rotational excitation energy of 24 meV for the quantum methyl rotor,[28] which is in excellent agreement with the measured value of 24.1 meV (Figure 9) observed with the VISION spectrometer.

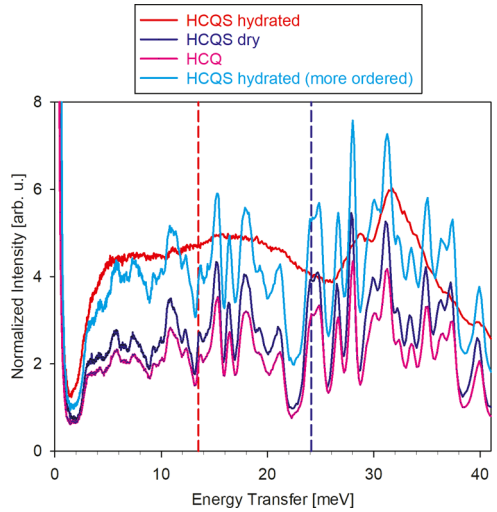

Figure 9. INS data from Figure 4 for dry HCQS (blue), main hydrated HCQS (red), free base HCQ (pink, scaled to the same mole values as the other two samples), and more ordered hydrated HCQS (cyan), in the region of the spectrum showing methyl group rotational excitations. The vertical dashed blue line at 24.1 meV is in excellent agreement with the value predicted from the activation energy of 10.7 kJ/mol. The vertical dashed red line at 13.5 meV is the value predicted from the activation energy of 3.8 kJ/mol.

The free base HCQ and more ordered hydrated HCQS also show the methyl rotation peak at the same position, in agreement with their similar activation energies (for the broad dynamic component) presented in Figure 7. However, there are no rotational peaks visible in Figure 9 for the main hydrated HCQS at 13.5 meV, as one would predict for the quantum methyl rotor[28] from the activation energy of 3.8 kJ/mol, or 39 meV, determined from the Arrhenius plot for the broad dynamic component in Figure 7. The rotational peak at 24 meV, characteristic of HCQ and dry HCQS, is also not present in the main hydrated HCQS spectrum. This suggests that, unlike in the

https://dx.doi.org/10.1021/acsomega.0c03091
ACS Omega 2020, 5, 21231−21240

more ordered hydrated HCQS, the hydration water likely randomizes the barriers for the methyl group rotations in the main hydrated HCQS, which thus can no longer be described in the framework of the methyl quantum rotations. Distribution of the barriers for the methyl group rotations does not give rise to a well-defined peak in the vibrational spectra. Yet, the effective average activation energies for the stochastic methyl rotation processes can still be measured by QENS, as presented in Figure 7. The data in Figure 7 show reduced activation energy (slope) for the main and less ordered hydration samples. In contrast, the corresponding prefactor (intercept) concurrently increases, suggesting that barrier randomization could have increased the average rate of methyl rotation in the higher-temperature range, above physiological temperatures.

Neither the introduction to HCQ of the sulfate groups to produce HCQS, nor the hydration of HCQS in the more ordered hydrated sample, results in a similar smearing effect on the methyl group rotations, as the rotational peak at 24 meV remains unchanged among HCQ, dry HCQS, and the more ordered hydrated HCQS, and the corresponding measured activation energies change only slightly (Figure 7). This suggests that the effect of hydration on the activation energy for the methyl group rotation may be due to the disorder introduced by the water molecules in the main hydrated and less ordered hydrated HCQS samples. It is thus instructive to compare the temperature dependence of the EISF for the dry and main hydrated HCQS samples (Figure S7). The EISF for the dry HCQS is temperature-independent, demonstrating that for the methyl group rotations, the jump rate is temperature-dependent (with an activation energy of 10.7 kJ/mol). In contrast, the number of methyl groups participating in the rotation is temperature-independent. Such behavior is typical for the functional groups in ordered systems. On the other hand, the EISF for the main hydrated HCQS sample is temperature-dependent. Thus, while the jump rate of the methyl groups becomes much less temperature-dependent in the main hydrated HCQS (with an activation energy of just 3.8 kJ/mol), the number of methyl groups participating in the rotation decreases as the temperature is reduced. The fraction of the immobile hydrogens in the system is defined by the "immobile" parameter c in the EISF(Q) fits with eq 3. When the temperature is decreased to 275 K, the parameter c, that is, the plateau value of the EISF(Q) for the main hydrated HCQS, coincides with that for the dry HCSQ, indicating that all of the hydration water molecules, which are fully mobile at 310 K, have become immobilized. The temperature dependence of the fraction of the immobilized water molecules in the main hydrated HCQS sample is shown in Figure S8. Therefore, the strong temperature dependence of the $\langle u^2(T)\rangle$ exhibited in Figure S4 by the main hydrated HCQS sample above ~250 K (in the absence of bulklike water freezing at 273 K) is driven primarily by changing with the temperature fraction of the immobilized water molecules. Such behavior is typical for the disordered hydration water.

To further describe the water in the main hydrated HCQS, we performed temperature-dependent measurements of the INS spectra using the SEQUOIA spectrometer. While the upper panels of Figures 10 and 11 show the measured spectra, the lower panels present a comparison of the difference spectra between the main hydrated and dry HCQS samples to the spectra of H_2O ice-Ih (5 K) and liquid water (295 K) as well as the structural H_2O in $WO_3{\cdot}H_2O$ data.[29] In Figure 10, the peaks at ~372 meV are mainly due to C−H and N−H stretching

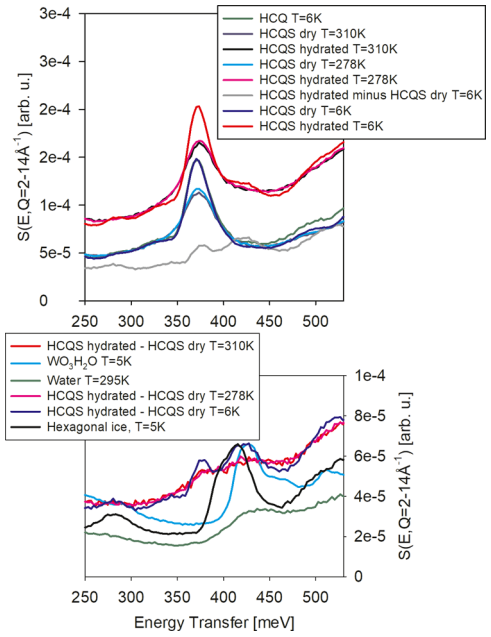

Figure 10. SEQUOIA wave-vector-integrated INS spectra collected with an incident energy of 600 meV. The Q-integration range is indicated in the vertical axis.

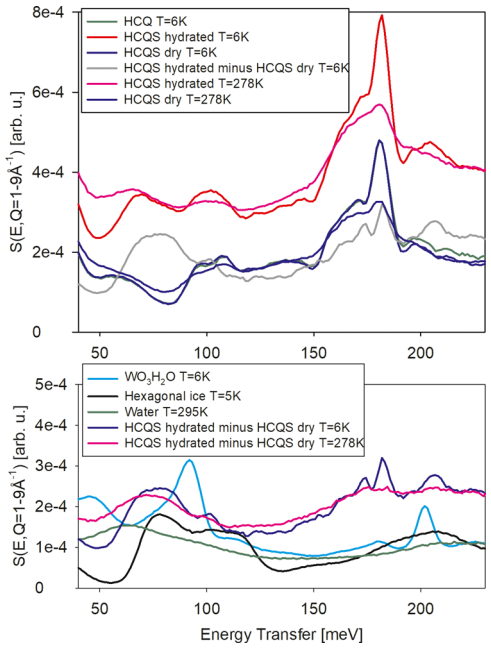

Figure 11. SEQUOIA wave-vector-integrated INS spectra collected with an incident energy of 250 meV. The Q-integration range is indicated in the vertical axis.

modes, and the shoulder at ~420 meV in the main hydrated HCQS sample spectra is due to O−H stretching modes of the hydration water (this peak is prominent in the difference spectrum at 6 K). At 6 K, the peak at ~372 meV can be fitted with two Gaussians, centered at 369 and 380 meV for the dry HCQS sample and 369 and 376 meV for the main hydrated HCQS sample. Due to the mismatch in the second peak position, the difference (hydrated—dry) HCQS spectrum shows a peak at 377 meV, whereas another peak in the difference spectrum (419 meV) is due to O−H stretching modes of the hydration water. The lower panel demonstrates that at 6

https://dx.doi.org/10.1021/acsomega.0c03091
ACS Omega 2020, 5, 21231−21240

K, the O−H stretching peak in the difference spectrum is broad, as it covers the peak in ice-Ih at its low-energy side and the peak of the structural water at its high-energy side. Therefore, the water in the main hydrated HCQS sample exhibits a distribution of hydrogen bonds, which are spread in strength from those observed in ice-Ih to the weaker bonds.

The spectra for the hydrated sample at 278 and 310 K almost coincide. The O−H stretching modes in the difference spectra decrease in intensity (due to the Debye−Waller factor) and do not shift (419 meV) or broaden, whereas the peak in liquid water at 295 K (431 meV) moves to much higher energy. This suggests that the water molecules at temperatures of 278−310 K are still confined and not in the bulk-like liquid state.

The spectra presented in Figure 11 show a sharp peak at about 181 meV due to C−H bending modes. The spectrum of the main hydrated HCQS sample shows a slight shift in the peak to higher energy and a new peak at ∼205 meV. Due to the change in the 181 meV peak, the difference HCQS spectrum (hydrated—dry) shows a minimum at 177 meV and a maximum at 182 meV. The peak at ∼205 meV is due to the intramolecular water H−O−H bending (or scissor) mode. At higher temperatures (278 K), the intensity of the bending H−O−H mode peak sharply decreased (due to the Debye−Waller factor).

In addition, the difference spectrum clearly shows a band between 60 and 120 meV, which can be assigned to librational vibrations of water. The lower panel of Figure 11 shows that at 6 K, this band is similar to the band in ice-Ih, and its characteristic sharp low-energy cutoff is shifted to lower energy by about 5 meV compared to that in ice-Ih. Therefore, the average hydrogen bonds in the confined water are weaker than in ice-Ih, which agrees with the stretching modes. At 278 K, the librational peak in the difference spectrum softens (compared to 6 K), but it is located at higher energy than in liquid water. Thus, the hydrogen bonds acting on the confined water in the main HCQS sample are larger in size than those in liquid water. The structural water (as in the $WO_3{\cdot}H_2O$ data,[29] also shown in the figure) exhibits sharper peaks in this range. Therefore, the appearance of the broad librational band is indicative of a disordered water network around the HCQS molecules.

CONCLUSIONS

Hydration water molecules may exert a profound influence on the dynamics of methyl group rotations in HCQS, in particular, by randomizing the potential barriers in a more disordered hydration structure. When the hydration results in a highly ordered structure similar to that of dry HCQS, the water molecules move in correlation with the other structural units, such as methyl groups, and do not alter the activation energy associated with the methyl group rotations. However, this changes when the hydration leads to a more disordered structure. Such a hydration state, which is more relevant to the state of HCQS in aqueous environments, randomizes and, on average, lowers the activation barriers for the methyl group rotations, even at minimal hydration levels. The modification of the potential barriers experienced by the HCQS methyl groups in the more disordered hydrated state could have implications for the function of the drug. It has been known that the introduction of methyl groups can dramatically increase the potency of drug molecules, sometimes by 3 orders of magnitude.[30−38] A boost in the drug efficiency by methyl groups is typically attributed to the altered binding affinity, solubility, or metabolism. On the other hand, it has been argued[39] that a critical advantage of methyl groups in biochemical processes is due to the ease of the thermally activated dynamics that increases the configurational entropy of the molecule and allows for more efficient sampling of the energy landscape,[40] which is crucial for biochemical activity. In this paradigm, further reduction of the activation energy for methyl group rotation would be beneficial to the drug function and efficiency. In contrast to the dry HCQS, or the HCQS in the ordered hydration state, the HCQS in the disordered hydration state experiences further plasticization of the methyl group dynamics via a randomized energy landscape and lowered, on average, potential barriers for rotations, analogous to the plasticizing effect of hydration water in proteins. This effect is remarkably pronounced already at minimal hydration levels of just four water molecules per HCQS structural unit. Therefore, the potential barriers and the associated stochastic dynamics of the methyl side groups could be significantly reduced in a disordered hydration environment experienced by the drug molecules *in vivo*.

EXPERIMENTAL AND COMPUTATIONAL METHODS

HCQS powder was purchased from Sigma-Aldrich and used as received for the preparation of liquid and solid samples. Aqueous D_2O solutions of HCQS at 20 and 40 mg/mL were loaded in flat-plate aluminum gold-coated sample holders of 50 mm height, 30 mm width, and 0.5 mm thickness, which were sealed hermetically using indium wire. The use of gold-coated sample holders was necessitated by the mildly corrosive character of the liquid samples. For the solid samples, hermetically sealed with indium wire sample holders of 1.0 mm thickness were used.

The backscattering BASIS spectrometer[20] provided a range of neutron energy transfers suitable for data analysis between −100 μeV and +100 μeV, with an energy resolution (averaged over all scattering angles) of 3.7 μeV full width at half maximum (FWHM). Routine data reduction procedures were used, including background subtraction and normalization to a vanadium standard. The quasielastic neutron scattering (QENS) measurements were performed at 310, 305, 290, and 275 K. In addition, continuous data collection occurred during a controlled cooling of 0.5 K/min. The sample-dependent resolution spectra were collected at a baseline temperature of 20 K. The SEQUOIA spectrometer[21] was used to measure inelastic neutron scattering (INS) data at incident neutron energies (E_i) of 250 and 600 meV, to provide an energy resolution of 2−3% for INS data below 550 meV and a momentum transfer (Q) between 1 and 14 Å^{-1}. The collected neutron scattering data were transformed from time-of-flight (TOF) and instrument coordinates to the dynamical structure factor $S(Q, E)$. INS data was also collected for the empty container under the same conditions and subtracted. The VISION spectrometer[22] was used to collect INS data over a broad energy-transfer range with a high-energy resolution ($\Delta E/E < 1.5\%$). Additional measurements were performed using the cold neutron chopper spectrometer (CNCS)[23] with an incident energy of 3.32 meV.

Density functional theory (DFT) was used to calculate the normal vibrational modes and INS spectra of dry HCQS using VASP.[41] The initial structure[13] was obtained from the CCDC (287809). The calculations used the projector augmented wave (PAW) approach[42,43] to describe the effects of the core electrons using the PBE exchange-correlation functional[44] and an optB86b-vdW functional for dispersion correction.[45] An energy cutoff of 800 eV was used for the plane-wave basis of the valence

https://dx.doi.org/10.1021/acsomega.0c03091
ACS Omega 2020, 5, 21231−21240

electrons. The electronic structure was calculated on a 2 × 3 × 1 Γ-centered grid. Given the relatively large unit cell (a = 10.5458 Å, b = 8.85 Å, c = 22.0826 Å), a large number of k points was not required to achieve convergence. We tested 2 × 3 × 1 and 3 × 4 × 1 grids, and the difference in the final energy was rather small (<0.1 meV). The vibrational spectra were also confirmed to be almost identical. The maximum interatomic force after optimization was below 0.001 eV/Å using a total energy tolerance of 10^{-8} eV for the electronic energy minimization and 10^{-7} eV for the structure optimization. The vibrational eigenfrequencies and normal modes were then calculated by solving the force constants and dynamical matrix using Phonopy.[46] The OCLIMAX software[47] was used to convert the DFT phonon results to the simulated INS spectra appropriate for comparison with each experimental measurement. To directly calculate the energy barrier associated with individual methyl group rotations, the climbing image nudged elastic band (cNEB) method[48] was used. Seven intermediate images were introduced, with the starting and the ending images being the two equilibrium positions of the methyl rotor separated by a relative rotation of 120°. We note that there are two nonequivalent methyl groups in the unit cell, and the energy barriers are close, with the lower one being 138 meV. The excitation energies for the quantum methyl rotor were solved using the Data Analysis and Visualization Environment (DAVE).[28]

■ ASSOCIATED CONTENT

Supporting Information

The Supporting Information is available free of charge at https://pubs.acs.org/doi/10.1021/acsomega.0c03091.

Diffusivity of HCQS in aqueous solutions; neutron diffraction patterns from the solid samples; mean-squared displacements (MSD) in the solid samples; QENS broadening in the dry and main hydrated solid samples; hydration water dynamics in the more ordered hydrated solid sample; temperature dependence of the EISF(Q) measured at BASIS for the dry and main hydrated solid samples; temperature dependence of the fraction of immobilized water molecules in the main hydrated sample (PDF)

■ AUTHOR INFORMATION

Corresponding Author

Eugene Mamontov − *Neutron Scattering Division, Oak Ridge National Laboratory, Oak Ridge, Tennessee 37831, United States;* orcid.org/0000-0002-5684-2675; Email: mamontove@ornl.gov

Authors

Yongqiang Cheng − *Neutron Scattering Division, Oak Ridge National Laboratory, Oak Ridge, Tennessee 37831, United States;* orcid.org/0000-0002-3263-4812

Luke L. Daemen − *Neutron Scattering Division, Oak Ridge National Laboratory, Oak Ridge, Tennessee 37831, United States*

Jong K. Keum − *Neutron Scattering Division, Oak Ridge National Laboratory, Oak Ridge, Tennessee 37831, United States*

Alexander I. Kolesnikov − *Neutron Scattering Division, Oak Ridge National Laboratory, Oak Ridge, Tennessee 37831, United States;* orcid.org/0000-0003-1940-4649

Daniel Pajerowski − *Neutron Scattering Division, Oak Ridge National Laboratory, Oak Ridge, Tennessee 37831, United States*

Andrey Podlesnyak − *Neutron Scattering Division, Oak Ridge National Laboratory, Oak Ridge, Tennessee 37831, United States*

Anibal J. Ramirez-Cuesta − *Neutron Scattering Division, Oak Ridge National Laboratory, Oak Ridge, Tennessee 37831, United States;* orcid.org/0000-0003-1231-0068

Matthew R. Ryder − *Neutron Scattering Division, Oak Ridge National Laboratory, Oak Ridge, Tennessee 37831, United States;* orcid.org/0000-0002-1363-8148

Matthew B. Stone − *Neutron Scattering Division, Oak Ridge National Laboratory, Oak Ridge, Tennessee 37831, United States*

Complete contact information is available at: https://pubs.acs.org/10.1021/acsomega.0c03091

Notes

The authors declare no competing financial interest.

■ ACKNOWLEDGMENTS

The neutron scattering experiments at Oak Ridge National Laboratory's (ORNL's) Spallation Neutron Source (SNS) were supported by the Scientific User Facilities Division, Office of Science (Basic Energy Sciences), US Department of Energy (DOE). This research project also benefited from the capabilities provided by the user program at the Center for Nanophase Materials Sciences (CNMS), a DOE Office of Science User Facility operated by ORNL. The authors acknowledge the US Department of Energy (DOE) Office of Science (Basic Energy Sciences) for research funding. M.R.R. acknowledges the National Energy Research Scientific Computing Center (NERSC), a US Department of Energy (DOE) Office of Science User Facility, operated under Contract No. DE-AC02−05CH11231, for access to supercomputing resources. Computing resources were also made available through the VirtuES and the ICEMAN projects, funded by Laboratory Directed Research and Development program at ORNL. We thank R. Moody for the dedication to obtaining sample materials. The authors also thank Dr. Jessica V. Lamb for assistance with the structural representations and Dr. Mark D. Lumsden for valuable discussion. This manuscript has been authored by UT-Battelle, LLC, under contract DE-AC05−00OR22725 with the US Department of Energy (DOE). The US Government retains and the publisher, by accepting the article for publication, acknowledges that the US government retains a nonexclusive, paid-up, irrevocable, worldwide license to publish or reproduce the published form of this manuscript or allow others to do so, for US government purposes. DOE will provide public access to these results of federally sponsored research in accordance with the DOE Public Access Plan (http://energy.gov/downloads/doe-public-access-plan).

■ REFERENCES

(1) Rainsford, K. D.; Parke, A. L.; Clifford-Rashotte, M.; Kean, W. F. Therapy and pharmacological properties of hydroxychloroquine and chloroquine in treatment of systemic lupus erythematosus, rheumatoid arthritis and related diseases. *Inflammapharmacology* **2015**, *23*, 231−269.

(2) Wang, Y.; Shi, K.; Zhang, L.; Hu, G.; Wan, J.; Tang, J.; Yin, S.; Duan, J.; Qin, M.; Wang, N.; Xie, D.; Gao, X.; Gao, H.; Zhang, Z.; He, Q. Significantly enhanced tumor cellular and lysosomal hydroxychlor-

oquine delivery by smart liposomes for optimal autophagy inhibition and improved antitumor efficiency with liposomal doxorubicin. *Autophagy* **2016**, *12*, 949−962.
(3) Zhang, H.; Ren, Y.; Cao, F.; Chen, J.; Chen, C.; Chang, J.; Hou, L.; Zhang, Z. In situ autophagy disruption generator for cancer theranostics. *ACS Appl. Mater. Interfaces* **2019**, *11*, 29641−29654.
(4) Al-Bari, M. A. A. Targeting endosomal acidification by chloroquine analogs as a promising strategy for the treatment of emerging viral diseases. *Pharmacol. Res. Perspect.* **2017**, *5*, No. e00293.
(5) Juurlink, D. N. Safety conciderations with chloroquine, hydroxychloroquine and azithromycin in the management of SARS-CoV-2 infection. *Can. Med. Assoc. J.* **2020**, *192*, E450−E453.
(6) Meyerowitz, E. A.; Vannier, A. G. L.; Friesen, M. G. N.; Schoenfeld, S.; Gelfand, J. A.; Callahan, M. V.; Kim, A. Y.; Reeves, P. M.; Poznansky, M. C. Rethinking the role of hydroxychloroquine in the treatment of COVID-19. *FASEB J.* **2020**, *34*, 6027−6037.
(7) Cortegiani, A.; Ingoglia, G.; Ippolito, M.; Giarratano, A.; Einav, S. A systematic review on the efficacy and safety of chloroquine for the treatment of COVID-19. *J. Crit. Care* **2020**, *57*, 279−283.
(8) MacIntyre, A. C.; Cutler, D. J. Role of lysosomes in hepatic accumulation of chloroquine. *J. Pharm. Sci.* **1988**, *77*, 196−199.
(9) Cutler, D. J. Possible mechanisms of action of antimalarials in rheumatic disease. *Agents Actions Suppl.* **1993**, *44*, 139−143.
(10) Rupley, J. A.; Careri, G. Protein hydration and function. *Adv. Protein Chem.* **1991**, *41*, 37−172.
(11) Hussain, T.; Kamarthapu, V.; Kruparani, S. P.; Deshmukh, M. V.; Sankaranarayanan, R. Mechanistic insights into cognate substrate discrimination during proofreading in translation. *Proc. Natl. Acad. Sci. U.S.A.* **2010**, *107*, 22117−22121.
(12) Allen, T. W.; Andersen, O. S.; Roux, B. On the importance of atomic fluctuations, protein flexibility, and solvent in ion permeation. *J. Gen. Physiol.* **2004**, *124*, 679−690.
(13) Semeniuk, A.; Kalinowska-Tluscik, J.; Nitek, W.; Oleksyn, B. J. Intermolecular interactions in crystalline hydroxychloroquine sulfate in comparison with those in selected antimalarial drugs. *J. Chem. Crystallogr.* **2008**, *38*, 333−338.
(14) https://pubchem.ncbi.nlm.nih.gov/compound/hydroxychloroquine.
(15) https://www.selleckchem.com/products/hydroxychloroquine-sulfate.html.
(16) Mamontov, E. Observation of fragile-to-strong liquid transition in surface water in CeO_2. *J. Chem. Phys.* **2005**, *123*, No. 171101.
(17) Caliskan, G.; Briber, R. M.; Thirumalai, D.; Garcia-Sakai, V.; Woodson, S. A.; Sokolov, A. P. Dynamic transition in tRNA is solvent induced. *J. Am. Chem. Soc.* **2006**, *128*, 32−33.
(18) Khodadadi, S.; Roh, J. H.; Kisliuk, A.; Mamontov, E.; Tyagi, M.; Woodson, S. A.; Briber, R. M.; Sokolov, A. P. Dynamics of biological macromolecules: Not a simple slaving by hydration water. *Biophys. J.* **2010**, *98*, 1321−1326.
(19) Mamontov, E.; Vlcek, L.; Wesolowski, D. J.; Cummings, P. T.; Rosenqvist, J.; Wang, W.; Cole, D. R.; Anovitz, L. M.; Gasparovic, G. Suppression of the dynamic transition in surface water at low hydration levels: A study of water on rutile. *Phys. Rev. E* **2009**, *79*, No. 051504.
(20) Mamontov, E.; Herwig, K. W. A time-of-flight backscattering spectrometer at the Spallation Neutron Source, BASIS. *Rev. Sci. Instrum.* **2011**, *82*, No. 085109.
(21) Granroth, G. E.; Kolesnikov, A. I.; Sherline, T. E.; Clancy, J. P.; Ross, K. A.; Ruff, J. P. C.; Gaulin, B. D.; Nagler, S. E. SEQUOIA: A newly operating chopper spectrometer at the SNS. *J. Phys.: Conf. Ser.* **2010**, *251*, No. 012058.
(22) https://neutrons.ornl.gov/vision.
(23) Ehlers, G.; Podlesnyak, A. A.; Niedziela, J. L.; Iverson, E. B.; Sokol, P. E. The new cold neutron chopper spectrometer at the Spallation Neutron Source: Design and performance. *Rev. Sci. Instrum.* **2011**, *82*, No. 085108.
(24) Perez, J.; Zanotti, J.-M.; Durand, D. Evolution of the internal dynamics of two globular proteins from dry powder to solution. *Biophys. J.* **1999**, *77*, 454−469.
(25) Wang, H.-W.; DelloStritto, M. J.; Kumar, N.; Kolesnikov, A. I.; Kent, P. R. C.; Kubicki, J. D.; Wesolowski, D. J.; Sofo, J. O. Vibrational density of states of strongly H-bonded interfacial water: Insights from inelastic neutron scattering and theory. *J. Phys. Chem. C* **2014**, *118*, 10805−10813.
(26) Bée, M. *Quasielastic Neutron Scattering*; Hilger: Bristol, 1988.
(27) Wuttke, J. Multiple-scattering effects on smooth neutron-scattering spectra. *Phys. Rev. E* **2000**, *62*, 6531−6539.
(28) Azuah, R. T.; Kneller, L. R.; Qiu, Y.; Tregenna-Piggott, P. L. W.; Brown, C. M.; Copley, J. R. D.; Dimeo, R. M. DAVE: A comprehensive software suite for the reduction, visualization, and analysis of low energy neutron spectroscopic data. *J. Res. Natl. Inst. Stand. Technol.* **2009**, *114*, 341−358.
(29) Mitchell, J. B.; Geise, N. R.; Paterson, A. R.; Osti, N. C.; Sun, Y.; Fleischmann, S.; Zhang, R.; Madsen, L. A.; Toney, M. F.; Jiang, D.; Kolesnikov, A. I.; Mamontov, E.; Augustyn, V. Confined interlayer water promotes structural stability for high-rate electrochemical proton intercalation in tungsten oxide hydrates. *ACS Energy Lett.* **2019**, *4*, 2805−2812.
(30) Belshaw, P. J.; Schoepfer, J. G.; Liu, K.-Q.; Morrison, K. L.; Schreiber, S. L. Rational design of orthogonal receptor-ligand combinations. *Angew. Chem., Int. Ed.* **1995**, *34*, 2129−2132.
(31) Shogren-Knaak, M. A.; Alaimo, P. J.; Shokat, K. M. Recent advances in chemical approaches to the study of biological systems. *Annu. Rev. Cell Dev. Biol.* **2001**, *17*, 405−433.
(32) Barreiro, E. J.; Kummerle, A. E.; Fraga, C. A. M. The Methylation Effect in Medicinal Chemistry. *Chem. Rev.* **2011**, *111*, 5215−5246.
(33) Quancard, J.; Bollbuck, B.; Janser, P.; Angst, D.; Berst, F.; Buehlmayer, P.; Streiff, M.; Beerli, C.; Brinkmann, V.; Guerini, D.; Smith, P. A.; Seabrook, T. J.; Traebert, M.; Seuwen, K.; Hersperger, R.; Bruns, C.; Bassilana, F.; Bigaud, M. A potent and selective S1P(1) antagonist with efficacy in experimental autoimmune encephalomyelitis. *Chem. Biol.* **2012**, *19*, 1142−1151.
(34) Leung, C. S.; Leung, S. S. F.; Tirado-Rives, J.; Jorgensen, W. L. Methyl effects on protein-ligand binding. *J. Med. Chem.* **2012**, *55*, 4489−4500.
(35) Schönherr, H.; Cernak, T. Profound methyl effects in drug discovery and a call for new C-H methylation reactions. *Angew. Chem., Int. Ed.* **2013**, *52*, 12256−12267.
(36) Fauber, B. P.; Rene, O.; Deng, Y. Z.; DeVoss, J.; Eidenschenk, C.; Everett, C.; Ganguli, A.; Gobbi, A.; Hawkins, J.; Johnson, A. R.; La, H.; Lesch, J.; Lockey, P.; Norman, M.; Ouyang, W. J.; Summerhill, S.; Wong, H. Discovery of 1-{4-[3-Fluoro-4-((3S,6R)−3-methyl-1,1-dioxo-6-phenyl-[1,2]thiazinan-2-ylmethyl)-phenyl]-piperazin-1-yl}-ethanone (GNE-3500): a potent, selective, and orally bioavailable retinoic acid receptor-related orphan receptor C (RORc or ROR gamma) inverse agonist. *J. Med. Chem.* **2015**, *58*, 5308−5322.
(37) Cernak, T.; Dykstra, K. D.; Tyagarajan, S.; Vachal, P.; Krska, S. W. The medicinal chemist's toolbox for late stage functionalization of drug-like molecules. *Chem. Soc. Rev.* **2016**, *45*, 546−576. correction 46, 1760 (2017), doi: 10.1039/c7cs90023f
(38) Feng, K.; Quevedo, R. E.; Kohrt, J. T.; Oderinde, M. S.; Reilly, U.; White, M. C. Late-stage oxidative C(sp(3))-H methylation. *Nature* **2020**, *580*, 621−627.
(39) Nickels, J. D.; Curtis, J. E.; O'Neill, H.; Sokolov, A. P. Role of methyl groups in dynamics and evolution of biomolecules. *J. Biol. Phys.* **2012**, *38*, 497−505.
(40) Frauenfelder, H.; Chen, G.; Berendzen, J.; Fenimore, P. W.; Jansson, H.; McMahon, B. H.; Stroe, I. R.; Swenson, J.; Young, R. D. A unified model of protein dynamics. *Proc. Natl. Acad. Sci. U.S.A.* **2009**, *106*, 5129−5134.
(41) Kresse, G.; Furthmüller, J. Efficient iterative schemes for ab initio total-energy calculations using a plane-wave basis set. *Phys. Rev. B* **1996**, *54*, 11169−11186.
(42) Blöchl, P. E. Projector augmented-wave method. *Phys. Rev. B* **1994**, *50*, 17953−17979.
(43) Kresse, G.; Joubert, D. From ultrasoft pseudopotentials to the projector augmented-wave method. *Phys. Rev. B* **1999**, *59*, 1758−1775.

https://dx.doi.org/10.1021/acsomega.0c03091
ACS Omega 2020, 5, 21231−21240

(44) Perdew, J. P.; Burke, K.; Ernzerhof, M. Generalized gradient approximation made simple. *Phys. Rev. Lett.* **1996**, *77*, 3865−3868.
(45) Klimeš, J.; Bowler, D. R.; Michaelides, A. Chemical accuracy for the van der Waals density functional. *J. Phys.: Condens. Matter* **2010**, *22*, No. 022201.
(46) Togo, A.; Tanaka, I. First principles phonon calculations in materials science. *Scr. Mater.* **2015**, *108*, 1−5.
(47) Cheng, Y. Q.; Daemen, L. L.; Kolesnikov, A. I.; Ramirez-Cuesta, A. J. Simulation of inelastic neutron scattering spectra using OCLIMAX. *J. Chem. Theory Comput.* **2019**, *15*, 1974−1982.
(48) Henkelman, G.; Uberuaga, B. P.; Jónsson, H. A climbing image nudged elastic band method for finding saddle points and minimum energy paths. *J. Chem. Phys.* **2000**, *113*, 9901−9904.

https://dx.doi.org/10.1021/acsomega.0c03091
ACS Omega 2020, 5, 21231−21240